photonics

MDPI

Article

Structured-Light Volume Measurement of Yarn Cheeses via Rotation-Axis-Constrained Shared-Cross-Section Registration

Chong Li, Yun Xu * and Jianbo Luo

School of Information Science and Engineering, Zhejiang Sci-Tech University, Hangzhou 310018, China
* Correspondence: ntxuyun@zstu.edu.cn

Abstract

Multi-view point cloud registration is challenging for yarn cheeses because their nearly axisymmetric geometry often leads to ambiguous point correspondences, particularly in regions with limited overlap and irregular surface contours. To address this problem, we propose rotation-axis-constrained shared-cross-section registration (RA-SCR) for structured-light volume measurement. The main contribution is a coupled pose–profile optimization method that jointly refines the three-degree-of-freedom residual pose of each view and a shared, axially layered cross-sectional model. Unlike approaches that use fitted geometric features only for initialization or keep them fixed during registration, RA-SCR updates the view-specific poses, shared center, and layer radii within the same robust optimization objective. Spatial correspondence residuals provide the information required for angular alignment, while layered radial residuals constrain the common axial profile across views. The resulting point clouds are used to estimate total package volume by axial–radial integration, from which the wound-yarn volume is obtained by subtracting the bobbin volume. In controlled comparisons, joint optimization reduced the radius-profile RMSE from 0.0702 to 0.0623 mm and the volume error from 0.3870% to 0.2914% relative to a fixed layered baseline. Additional low-overlap and initialization-perturbation tests yielded a registration success rate of 87.2% compared with 84.6% for fixed layered radii and 66.7% for conventional 6-DoF ICP. Across five yarn-cheese samples, the maximum relative errors were 3.4625% for total package volume and 2.8327% for wound-yarn volume.

Keywords: structured-light measurement; yarn cheese; rotation-axis constraint; shared-cross-sectional registration; point cloud registration; volume measurement

1. Introduction

Yarn-cheese geometry affects winding quality and downstream dyeing and finishing [1–3]. Reliable volume measurements are therefore useful for quality inspection and process control. Inaccurate volume estimates can obscure changes in package shape and limit their value for process optimization [4].

Yarn-cheese volume is commonly estimated with geometric approximations [5,6]. These are simple but may miss texture-dependent contours and irregular boundaries [7]. Manual and contact measurements also limit throughput and repeatability. Noncontact methods, including machine vision [8], laser scanning [9], simultaneous localization and mapping (SLAM) [10], and time-of-flight cameras [11], have expanded the options for measuring complex objects [12,13]. Structured light offers dense three-dimensional surface data for this application.

Check for updates

Received: 23 October 2026
Revised: 17 November 2026
Accepted: 18 November 2026
Published: 24 November 2026

Copyright: © 2026 by the authors. Licensee MDPI, Basel, Switzerland. This article is an open access article distributed under the terms and conditions of the Creative Commons Attribution (CC BY) license.

In fringe-projection structured light, a camera records patterns deformed by the object surface. Phase recovery, phase unwrapping [14–16], and triangulation yield a point cloud for each view. Phase processing governs single-view quality, while registration governs the consistency of the fused surface. Both affect the volume calculated from that surface.

Wang et al. proposed a single-frame super-resolution fringe projection three-dimensional imaging method, which recovered high-resolution absolute phase from low-resolution and low-signal-to-noise-ratio fringe images using deep learning, enabling high-speed three-dimensional imaging at 100,000 fps [17]. Zhao et al. addressed indirect-light interference in complex scenes by proposing a scene-adaptive pattern coding method for fringe projection. By adaptively controlling the projection region, the method suppressed non-diffuse reflection interference and achieved over 97% diffuse-region recognition accuracy among 100 scenes, reducing the plane-fitting root-mean-square error (RMSE) to 56.84 μm [18].

Point-cloud registration methods based on geometric constraints and learned features have been extensively investigated. Qin et al. proposed GeoTransformer, which encodes geometric relationships such as point distances and angles using Transformer architectures to improve feature matching under low-overlap conditions, achieving high registration accuracy on the KITTI dataset [19]. Yang et al. developed the maximal-cliques registration method (MAC) by constructing correspondence compatibility graphs and searching locally consistent maximal cliques to reduce the influence of incorrect correspondences on pose estimation. Combined with GeoTransformer, MAC achieved high recall rates on the 3DMatch and 3DLoMatch datasets [20]. Lv et al. used local circular cross-sections for coarse registration of laser scans of steel tubular arch segments, followed by coherent point drift (CPD) for refinement. In the proposed RA-SCR method, the calibrated turntable axis restricts each view to three residual pose parameters, while the view-specific poses, shared cross-sectional center, and axially layered radii are jointly optimized. Spatial correspondences constrain angular alignment, whereas the radial term promotes cross-view geometric consistency. The main contribution lies in this coupled optimization rather than circular fitting alone [21].

To address missing data and noise in structured-light measurements, Feng et al. proposed adaptive point cloud restoration and multi-view fusion strategies to improve reconstruction quality and registration continuity for highly reflective surfaces [22,23]. Lai et al. employed graph optimization to establish global consistency constraints among multiple frames, enhancing the automation and robustness of structured-light scanning [24]. Bao et al. reduced the influence of noise on geometric parameter extraction through robust fitting and cross-sectional modeling [25], while Ye et al. improved rotation-axis estimation accuracy in turntable-based structured-light systems using binocular vision calibration [26].

Li et al. proposed a contour extraction and edge completion method for structured-light point clouds with discreteness, noise, and missing boundary data. By incorporating geometric constraints to recover incomplete contours, the method improved blade parameter measurement accuracy, achieving an average absolute error below 0.120 mm on more than 200 blades [27]. Huang et al. developed a bidirectional line-structured-light scanning method with feature constraints to address incomplete blade cross-sectional profiles. By integrating bidirectional scanning data, the method reconstructed complete profiles and achieved high-precision maximum thickness measurement, with a maximum deviation of only 0.003 mm compared with coordinate measuring machine results [28].

Despite advances in phase recovery, calibration, and structured-light reconstruction, registering turntable views remains difficult. Similar local geometry on an approximately axisymmetric yarn cheese can produce false nearest-neighbor matches and contour drift. We therefore propose RA-SCR for yarn-cheese volume measurement. The calibrated turntable

axis provides a common coordinate system and limits residual pose optimization to three degrees of freedom. Layered cross-sectional radii add a shared geometric constraint. We combine the registered surface with axial–radial integration to estimate total package, bobbin, and wound-yarn volumes.

RA-SCR jointly estimates view-specific residual poses and a shared layered cross-section. The turntable axis restricts each pose correction to two in-plane translations and one axial rotation. Correspondences between adjacent views constrain rotation when their overlap is sufficient. A shared center and layer radii constrain the radial shape across views; this radial term alone cannot identify axial rotation.

2. Measurement Method and Principle

2.1. Monocular Fringe Projection Structured-Light System for Yarn-Cheese Volume Measurement

Yarn cheeses are approximately axisymmetric packages with textured surfaces, fiber fuzz, and irregular end boundaries. Texture and fuzz can disturb phase recovery and contour extraction, while occlusion leaves gaps in individual views. Similar contours can also produce false matches during registration. We address these issues with a monocular fringe-projection system comprising a projector, an industrial camera, and a turntable (Figure 1).

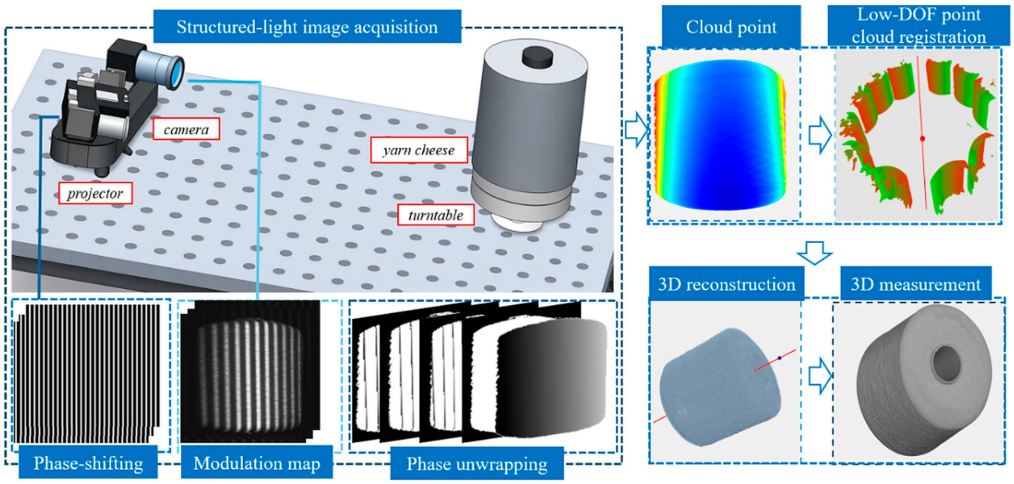


Figure 1. Schematic of the monocular fringe projection structured-light system for yarn-cheese volume measurement.

The projector displays multifrequency eight-step phase-shifting patterns, and the camera captures the deformed fringes under synchronized triggering (Figure 1). The turntable supplies side views at prescribed angles. Phase recovery and a modulation map identify valid regions; multifrequency unwrapping and calibrated triangulation then reconstruct each view. After turntable-axis calibration, RA-SCR aligns and fuses the side-view point clouds.

2.2. Rotation-Axis-Constrained Shared-Cross-Sectional Point Cloud Registration Method

The turntable axis defines the common coordinate system for registration. Cuboid side-face normals estimate its direction, and a local circle fit supplies an axial reference point. Residual alignment then optimizes two in-plane translations and one axial rotation per view. A layered cross-sectional model couples these poses to a shared center and radii through correspondence and radial residuals.

2.2.1. Rotation-Axis Direction Estimation of the Turntable Based on Cuboid Side-Face Normal Constraints

The turntable rotation axis is a fixed geometric property of the measurement system, remaining constant across different measurements as long as the system configuration is not altered. Estimating it directly from a yarn cheese is unreliable because texture and irregular ends can bias the fit. We instead calibrate its direction with the planar side faces of a cuboid reference and use that direction for all views (Figure 2).

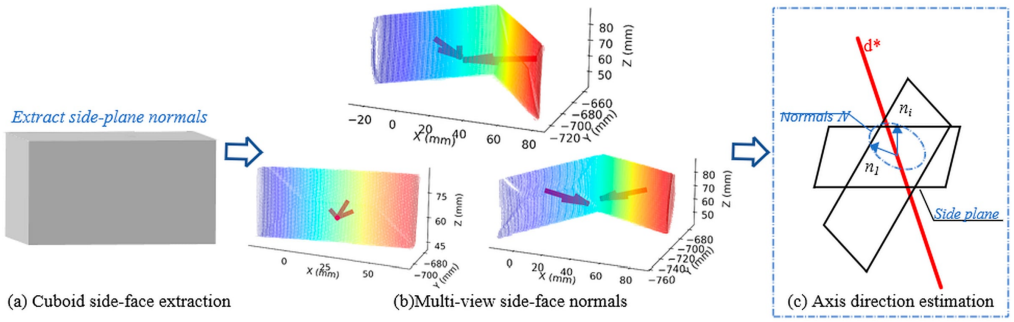


Figure 2. Estimation of the turntable rotation-axis direction using cuboid side-face normal constraints.

The side surfaces of the cuboid reference object can be approximately regarded as planar structures in the local point cloud, and their plane normal vectors theoretically satisfy an orthogonality relationship with the turntable rotation-axis direction. Therefore, the side-face normal vectors extracted at multiple rotation angles can be used as the constraints for rotation-axis direction estimation. Accordingly, random sample consensus (RANSAC) is employed to segment candidate side-face planes, and the corresponding candidate unit normal vectors are obtained by normalizing the coefficients of the plane models. Suppose the two candidate unit normal vectors extracted from a single-frame point cloud are n_1 and n_2, respectively. The angle between them is defined as:

$$\theta_{12} = \arccos\left(\left|\hat{n}_1^T \hat{n}_2\right|,\right)\ \theta_{12} \in [0°, 90°] \tag{1}$$

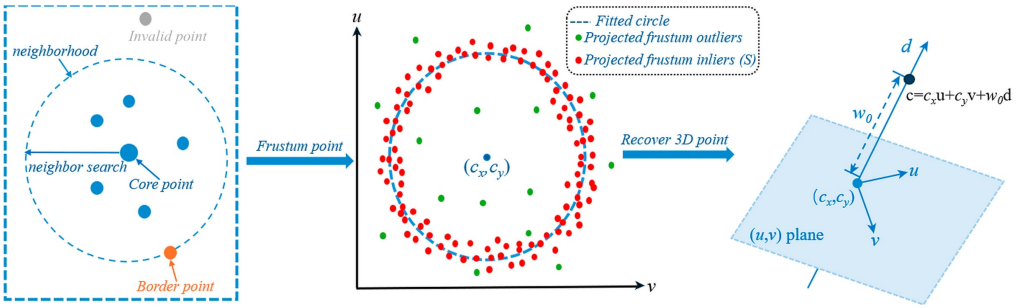
where θ_{12} is larger than the predefined threshold θ_0, the current frame is considered to contain two different valid side faces, and both normal constraints are retained. Otherwise, the two candidate planes are considered to be repeatedly extracted from the same side face. Because the angle between the normal vectors of adjacent cuboid side faces is theoretically close to 90°, whereas the angle between normal vectors repeatedly fitted from the same side face is close to 0°, $\theta_0 = 45°$ is selected as the discrimination threshold. Ideally, the turntable rotation-axis direction d is orthogonal to the side-face normal vectors n_j of the cuboid. Let the number of valid side-face normal vectors selected for rotation-axis estimation be m, where $m \geq 2$. Considering point cloud noise and normal estimation errors, all normal constraints are stacked into a matrix N to solve for the optimal rotation-axis direction.

$$d^* = \operatorname{argmin}_{\|d\|=1} \|Nd\|^2,\ N = \begin{bmatrix} \hat{n}_1^T & \hat{n}_2^T & \cdots & \hat{n}_m^T \end{bmatrix}^T \tag{2}$$

Singular value decomposition is performed on matrix N, and the right singular vector corresponding to the minimum singular value is selected as d^*. For subsequent coordinate projection and point cloud decomposition, the estimated rotation-axis direction is uniformly denoted as d.

2.2.2. Rotation-Axis Position Determination Based on Local Circular Cross-Sectional Fitting

An axis direction does not specify the axis position. Whole-cloud principal component analysis may be biased by uneven sampling and asymmetric yarn-cheese surfaces. We therefore locate a reference point by fitting a circle to a local cross-section (Figure 3).



(a) DBSCAN point cloud clustering (b) Cross-sectional circle fitting (c) 3D rotation-axis recovery

Figure 3. Point cloud clustering and circular cross-sectional fitting strategy.

To estimate the axis position, a local cross-section is isolated and projected onto the plane normal to the estimated axis, where a circle is fitted. The fitted center gives the transverse position of the axis, and its axial coordinate is recovered from the same local point set.

Step 1: To obtain the rotation center of the turntable, the point cloud is separated using density-based spatial clustering of applications with noise, and the circular turntable-layer point cloud is extracted. A local cross-sectional coordinate system is established on a plane perpendicular to the rotation-axis direction. Let d denote the rotation-axis direction vector. Two mutually orthogonal unit basis vectors u and v, which are orthogonal to d, are constructed. The projection of the 3D coordinate vector of an arbitrary point p_i in the extracted turntable layer onto the plane perpendicular to the rotation axis is defined as follows:

$$\begin{bmatrix} \tilde{x}_i \\ \tilde{y}_i \end{bmatrix} = \begin{bmatrix} u^T p_i \\ v^T p_i \end{bmatrix}, \; w_i = d^T p_i \tag{3}$$

where u and v are unit basis vectors orthogonal to the rotation-axis direction vector d; $(\tilde{x}_i, \tilde{y}_i)$ denotes the two-dimensional projection coordinates of point p_i on the cross-sectional plane perpendicular to the rotation-axis, and w_i represents the axial coordinate of point p_i along the rotation-axis direction.

Step 2: The RANSAC algorithm is applied to fit circles on the projected two-dimensional point set of the turntable-layer point cloud, obtaining the circle centers (c_x, c_y) at different heights. Here, a single (c_x, c_y) only describes the two-dimensional position of the corrected point in the cross-sectional plane perpendicular to the rotation axis. The exact position of the rotation center in 3D space still needs to be determined together with its axial coordinate.

Step 3: To recover the two-dimensional circle center as a spatial point, its position along the rotation-axis direction d must be further determined. Since the inlier set S involved in circle fitting is obtained from a local cross-sectional region of the same local turntable layer, its distribution along the rotation-axis direction is limited within a narrow range. Therefore, the axial coordinates w_i of the inliers are concentrated within a small interval. Let N_s denote the number of points in set S. The axial coordinate of the fitted circle center can be estimated by the arithmetic mean of the axial coordinates of the inliers:

$$w_0 = \frac{1}{N_s} \sum_{i=0}^{N_s - 1} w_i \tag{4}$$

Therefore, the two-dimensional circle center (c_x, c_y) provides the position in the cross-sectional plane, while w_0 provides the axial position. The two components together determine the 3D center point: $c = c_x u + c_y v + w_0 d$. The rotation axis can then be directly represented as a line passing through the reference point c with the direction vector d:

$$l(\lambda) = \left(c_x u + c_y v + w_0 d\right) + \lambda d \tag{5}$$

where $l(\lambda)$ represents the spatial rotation axis, and λ is the parameter of the axis line. The estimated rotation axis establishes a unified geometric reference frame for subsequent multi-view point cloud coarse alignment and rotation-axis-constrained fine registration.

The reliability of the estimated axis depends on the quality of the plane and circle fitting results. During axis-direction estimation, RANSAC was used to extract the cuboid side faces with a point-to-plane distance threshold of 1.5 mm. Plane candidates containing fewer than 300 inlier points were discarded, and a 45° threshold between the fitted normals was used to distinguish different side faces. These criteria help reduce the influence of outliers and repeated extraction of the same surface. Nevertheless, incomplete surface coverage, errors in circle fitting, and mechanical wobble of the turntable may still affect the estimated axis.

2.2.3. Cross-Sectional Residual Pose Parameter Estimation and Correction Under Rotation-Axis Constraints

Under the condition that the rotation-axis direction and axial position have been determined, the residual pose parameters of the k-th point cloud are defined by retaining two translational components $d_{x,k}$ and $d_{y,k}$ within the cross-sectional plane and an angular correction component $\Delta\theta_k$ around the rotation-axis, which can be expressed as:

$$\Delta\xi_k = [d_{x,k}, d_{y,k}, \Delta\theta_k]^T \tag{6}$$

At this stage, the single-view registration is reduced from the conventional six-degree-of-freedom rigid transformation optimization to a three-degree-of-freedom optimization within the cross-sectional plane, thereby reducing registration errors caused by incorrect correspondences and local contour drift in approximately axisymmetric yarn cheeses. The original point clouds in the world coordinate system are transformed into the axis coordinate system with the rotation axis defined as the Z_a-axis through translation and rotation operations, as illustrated in Figure 4.

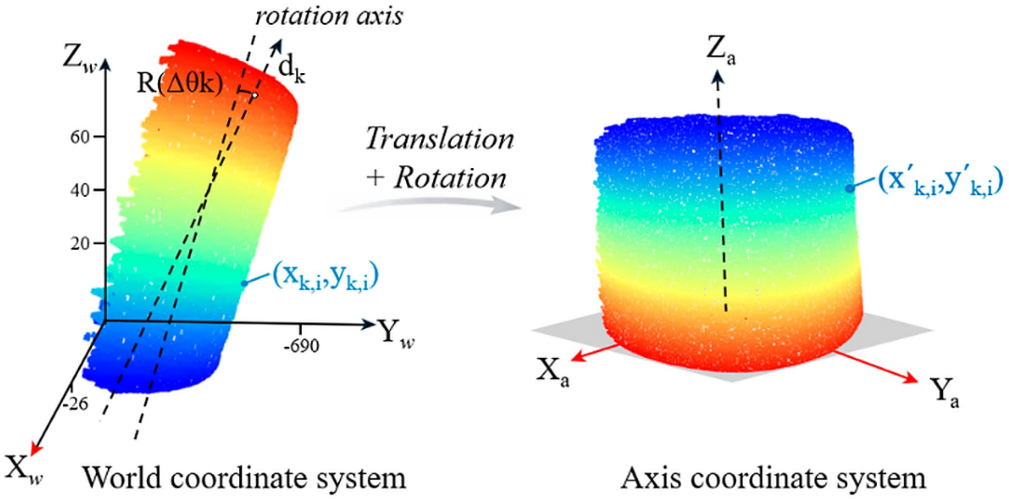


Figure 4. Schematic of the coordinate transformation of multi-view point clouds into the rotation-axis coordinate system.

Let $(x_{k,i}, y_{k,i})$ denote the cross-sectional coordinates of the i-th point in the k-th point cloud. The corrected coordinates after residual pose compensation are given by:

$$\begin{cases} x'_{k,i} = x_{k,i}\cos\Delta\theta_k - y_{k,i}\sin\Delta\theta_k + d_{x,k} \\ y'_{k,i} = x_{k,i}\sin\Delta\theta_k + y_{k,i}\cos\Delta\theta_k + d_{y,k} \end{cases} \tag{7}$$

The multi-view point clouds are first coarsely aligned according to the preset turntable rotation angles used during acquisition. The residual angular correction $\Delta\theta_k$ represents the small rotation error remaining around the rotation axis in the k-th view after coarse alignment and is estimated by minimizing the spatial correspondence residuals within the axially overlapping regions of adjacent views.

Following transformation into the rotation-axis coordinate system, the residual pose of each point-cloud frame is parameterized by two cross-sectional translations and a small rotation about the axis. These pose corrections are jointly optimized with the shared-cross-section parameters.

2.2.4. Shared-Cross-Sectional-Driven Multi-View Collaborative Optimization

Since the cross-sectional dimensions of the yarn cheese along the rotation-axis direction are not constant, using a single shared-cross-sectional radius to describe the overall geometric structure may neglect local contour variations and introduce systematic bias. Therefore, the shared-cross-sectional radius is extended from a single global parameter to a layered shared-cross-sectional radius model varying along the rotation-axis direction.

RA-SCR approximates each axial slice as circular. Its shared radius represents the dominant contour across views, not every surface point. The robust loss limits the influence of isolated fuzz and texture deviations. The approximation is reasonable when circumferential variations are small relative to the package radius. Pronounced ellipticity, persistent bulges, or asymmetric winding can instead introduce systematic shape and volume bias. Such samples require a direction-dependent cross-sectional model.

Specifically, the multi-view point clouds involved in optimization are uniformly divided into M cross-sectional regions along the axial direction. Let the m-th axial slice be denoted as S_m. The cross-sectional coordinates of point $p_{k,i}$ within this slice after the three-degree-of-freedom transformation are represented as $(x'_{k,i}, y'_{k,i})$, where (c_x, c_y) denotes the projection center of the rotation axis on the cross-sectional plane. The initial shared-cross-sectional radius of this slice is estimated as:

$$R_m^{(0)} = \text{median}\left(\sqrt{(x'_{k,i} - c_x)^2 + (y'_{k,i} - c_y)^2}\right),\ p_{k,i} \in S_m \tag{8}$$

The initialized radii are subsequently jointly optimized with the multi-view pose correction parameters.

The layered shared-cross-sectional radii of all axial slices are collectively represented as a radius parameter vector $R_s = [R_1,\ldots,R_m]^{\mathrm{T}}$. For the i-th point $p_{k,i}$ in the k-th point cloud, let $z_{k,i}$ denote its axial coordinate in the axis coordinate system, and let $m(k, i)$ represent the index of the axial slice to which the point belongs. The shared-cross-sectional radius corresponding to this point can then be obtained by indexing the radius parameter vector:

$$R_{m(k,i)} = R_s[m(k,i)] \tag{9}$$

Through this indexing relationship, all points are mapped to the shared-cross-sectional model, while local correspondences are retained to constrain the residual angular correction. The pose correction parameters defined in Equation (6) and the shared-cross-sectional radius parameters are jointly formulated as the optimization variables. The optimal variables are obtained as:

$$x^* = \text{argmin}_x E(x) \tag{10}$$

where R_s is the layered shared-cross-sectional radius vector defined above. These parameters collectively constitute the joint optimization variables for multi-view point clouds. According to Equation (7), the cross-sectional coordinates of the i-th point in the k-th point cloud are corrected from $(x_{k,i}, y_{k,i})$ to $(x'_{k,i}, y'_{k,i})$. The cross-sectional radial distance is determined by the distance between the corrected cross-sectional coordinates and the projection

center (c_x, c_y) of the rotation axis. If the point belongs to the $m(k,i)$-th axial slice, its ideal radial distance should be consistent with the shared-cross-sectional radius corresponding to that slice. Therefore, the difference between the actual radial distance of the corrected point and the shared-cross-sectional radius of its corresponding slice is constructed as the residual, which is used to characterize the geometric consistency deviation of multi-view point clouds under the shared-cross-sectional model.

In Equation (10), the joint variable x contains the three residual pose parameters (dx,k, dy,k, and Δθk) for each view, the shared cross-sectional center (cx, cy), and the shared radius vector Rs = (R1, ..., RM). Thus, the center is updated together with the view poses and the M layer radii. The rotation-axis direction is calibrated beforehand and is held fixed in this optimization.

To jointly constrain the residual angular correction and the layered radial consistency, the spatial correspondence residuals within the overlapping regions of adjacent views are combined with the shared-cross-section radial residuals. The Huber robust loss function is introduced to reduce the influence of incorrect correspondences, local missing regions, and outliers. The joint objective function is constructed as follows:

$$E(x) = \sum_{k,i,j} \sum_{q=1}^{3} \rho\left(\alpha_p \Delta p_{k,i,j,q}\right) + \sum_{k,i} \rho\left(\alpha_r \Delta r_{k,i}\right) \tag{11}$$

where c_k denotes the set of point correspondences established within the axially overlapping region between the k-th and $(k+1)$-th views after coarse registration, and j denotes the index of the point in the $(k+1)$-th view corresponding to the i-th point in the k-th view. The corrected 3D point is denoted by $p'_{k,i} = [x'_{k,i}, y'_{k,i}, z_{k,i}]^{\mathrm{T}}$, where $x'_{k,i}$ and $y'_{k,i}$ are calculated using Equation (7). The factors α_p and α_r are the spatial and radial residual multipliers, respectively. They act on scalar residuals before the Huber loss is evaluated. Their values balance the two terms of the objective.

In Equation (11), Δp(k,i,j,q) is coordinate q (q = 1, 2, 3) of the corrected point difference for correspondence (i,j) between adjacent views. Δr(k,i) is the corrected radial distance from (cx, cy) minus the radius R[m(k,i)] of that point's axial layer. The implemented Huber objective applies ρ to each scaled scalar residual. For the original real-scan reconstruction, the spatial and radial multipliers were 2.0 and 0.04, with 10 axial layers. The controlled held-out benchmark in Section 3.2.1 instead selected a radial multiplier of 0.20 and 16 layers on its validation split.

The radial residual is invariant to rotation about the calibrated axis and therefore cannot independently determine the axial rotation angle. The spatial correspondence residual provides the angular information required for relative pose estimation, while the layered radial residual constrains transverse translations and shared cross-sectional parameters. Combining these residuals enables simultaneous pose estimation and cross-sectional consistency optimization.

Conventional frame-by-frame point-to-point registration relies on local correspondences. In contrast, RA-SCR formulates the registration as a global optimization problem using layered shared-cross-sectional radii. For a unified description of the optimization process, the cross-sectional translation corrections $(d_{x,k}, d_{y,k})$, the small rotational correction $\Delta\theta_k$ around the rotation axis, the shared center (cx, cy), and the layered shared-cross-sectional radius parameters R_s shared by all views are collectively denoted as the joint optimization variable x. The above objective is further formulated as a robust nonlinear least-squares problem with respect to the joint optimization variable x, and the residual function is iteratively updated using first-order linearization:

$$e(x + \Delta x) \approx e(x) + J\Delta x \tag{12}$$

where J denotes the Jacobian matrix of the residuals with respect to the joint optimization variable x, and Δx represents the parameter increment in the current iteration. By incorporating the Huber robust loss function, Δx is solved using the weighted least-squares method, and the pose correction parameters and layered shared-cross-sectional radius parameters in Equation (10) are iteratively updated until the joint objective function converges.

Because the objective is invariant to a common transverse translation applied to all view translations and the shared center, two gauge freedoms are removed by imposing the symmetric constraints that the sums of Δxk and Δyk over all views are zero. The implementation enforces these equalities at every Gauss–Newton update through a constrained KKT solve. Consequently, (cx, cy) represents the common transverse offset relative to the calibrated axis, whereas (Δxk, Δyk) are zero-mean view-specific residual corrections. This constraint selects a unique parameterization without changing the correspondence residuals, radial residuals, relative registration, or calculated volume.

After completing the registration of the multi-view side-surface point clouds, the missing geometric information in the end regions caused by limited observation angles is compensated. While maintaining the position and rotation angle of the yarn cheese in the turntable coordinate system unchanged, the turntable is rotated to acquire the top and bottom point clouds of the yarn cheese. These point clouds are subsequently registered and fused, resulting in the complete 3D surface model of the yarn cheese.

2.3. Axial–Radial Layered Volume Calculation of the Yarn Cheese

Yarn texture and fiber fuzz can create erroneous connections in a triangulated surface. We therefore calculate the volume from axial slices rather than requiring a closed mesh. Representative slice radii define the outer profile; integration gives the total package volume. Subtracting the empty-bobbin volume gives the wound-yarn volume.

2.3.1. Extraction of End-Face Radius and Height

To obtain the end-face radius and height of the yarn cheese, a frustum parameter extraction workflow is designed, as shown in Figure 5.

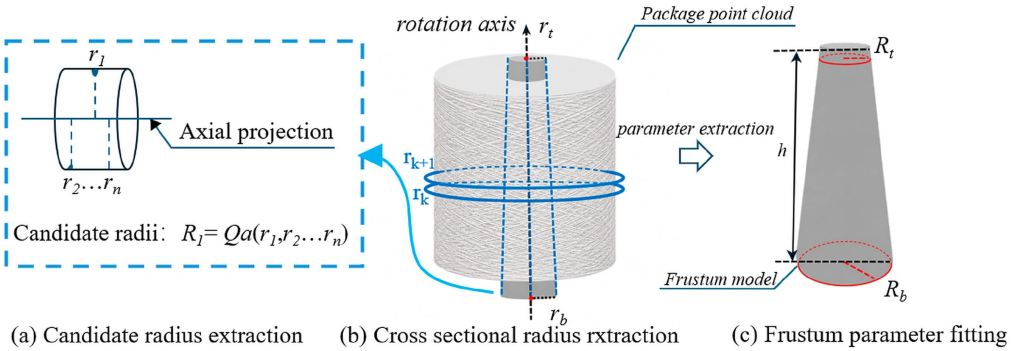


Figure 5. Workflow of the yarn-cheese frustum parameter extraction. (**a**) End-face radius calculation process of the yarn cheese; (**b**) axial segmentation of the point cloud and cross-sectional radius extraction based on the rotation axis; (**c**) frustum parameter fitting model of the yarn cheese.

Let p_i denote an arbitrary point in the point cloud, p_0 represent a reference point on the rotation-axis, and d denote the unit direction vector of the rotation-axis. The axial coordinate z_i of point p_i along the rotation-axis direction and the radial distance r_i from the point to the rotation axis can, respectively, be expressed as follows:

$$\begin{cases} z_i = (p_i - p_0)^T d \\ r_i = \|(p_i - p_0) - z_i d\|_2 \end{cases} \quad (13)$$

where z_i represents the projected coordinate value of the point along the rotation-axis direction, and r_i represents the distance between the point and the rotation axis. After this coordinate transformation, the original 3D point cloud is converted into an axial position–radial distance representation, which can directly characterize the contour variation of the yarn cheese along the axial direction. The effective axial coordinate values at the top and bottom of the yarn cheese are denoted as z_t and z_b, respectively. The height can then be calculated as:

$$h = z_t - z_b \tag{14}$$

Since the radial distances of points within a single slice are affected by surface fiber fuzz, local noise, and occlusion-induced missing data, directly using the maximum radius or average radius may lead to an overestimation of the contour or deviation from the actual boundary. Therefore, a quantile-based representative radius is adopted for each slice. For the k-th slice, the set of radial distances is denoted as R_k, and the quantile operator $Q_\alpha(\cdot)$ is used to extract the representative radius of this slice, where α is the quantile coefficient, and r_k denotes the representative radius of the k-th layer, which can be expressed as:

$$r_k = Q_\alpha(R_k) \tag{15}$$

A higher α traces the outer contour of the yarn body. A lower α reduces the influence of residual yarn near the tube end. In practice, α is selected within a predefined range using slice point count and radial variation to obtain a smooth profile and stable end-radius estimate.

For the empty-bobbin contour, we use a low quantile for the end slice. The experiments use the 15th percentile.

2.3.2. Volume Parameter Calculation of the Yarn Cheese

Since the yarn cheese contains an internal bobbin, directly calculating the volume by treating the entire point cloud as a solid of revolution only yields the total volume of the yarn cheese, which cannot represent the volume occupied by the yarn material itself. This study measures the yarn-cheese height, end radii, and total volume, calculates the empty-bobbin volume from its radii and effective height, and obtains the wound-yarn volume by subtracting the bobbin volume from the total volume.

Here, the bobbin is approximated as a frustum with different upper and lower end radii. The volume of the yarn bobbin is calculated according to the end radii and effective height, and the volume of the yarn material is subsequently obtained. Let r_t and r_b denote the upper and lower radii of the empty bobbin, respectively, and let h denote its effective axial height. The volume of the yarn bobbin V_b can be expressed as follows:

$$V_b = \frac{\pi h}{3}\left(r_t^2 + r_t r_b + r_b^2\right) \tag{16}$$

During the calculation, the point cloud is divided into N equally spaced axial slices along the rotation-axis direction. For each valid slice, the radial distances of points to the rotation axis are statistically analyzed, and the specified quantile is selected as the outer contour radius r_k of the corresponding slice. Subsequently, the cross-sectional areas of adjacent slices are accumulated using trapezoidal integration to obtain the total volume of the yarn cheese V_t, which can be written as follows:

$$V_t = \sum_{k=1}^{N-1} \frac{\pi\left(r_k^2 + r_{k+1}^2\right)}{2}\Delta z \tag{17}$$

Here, Δz represents the axial spacing between adjacent slices. Based on this, the wound-yarn volume V_w can be obtained from the total volume of the yarn cheese V_t and the volume of the yarn bobbin V_b, which can be expressed as:

$$V_w = V_t - V_b \tag{18}$$

3. Experiments and Results

3.1. Yarn-Cheese Volume Measurement System Based on Monocular Fringe Projection Structured Light

The measurement system consists of an SLM2010 projector, a Hikvision MV-CA016-10UC industrial camera (Hangzhou Hikrobot Co., Ltd., Hangzhou, China), and a circular turntable, as shown in Figure 6. To achieve synchronous control between pattern projection and image acquisition, the projector and camera are connected through a trigger line. When the projector projects the fringe patterns, the projector sends a high-level trigger signal through the trigger port, and the camera acquires an image after receiving the trigger signal.

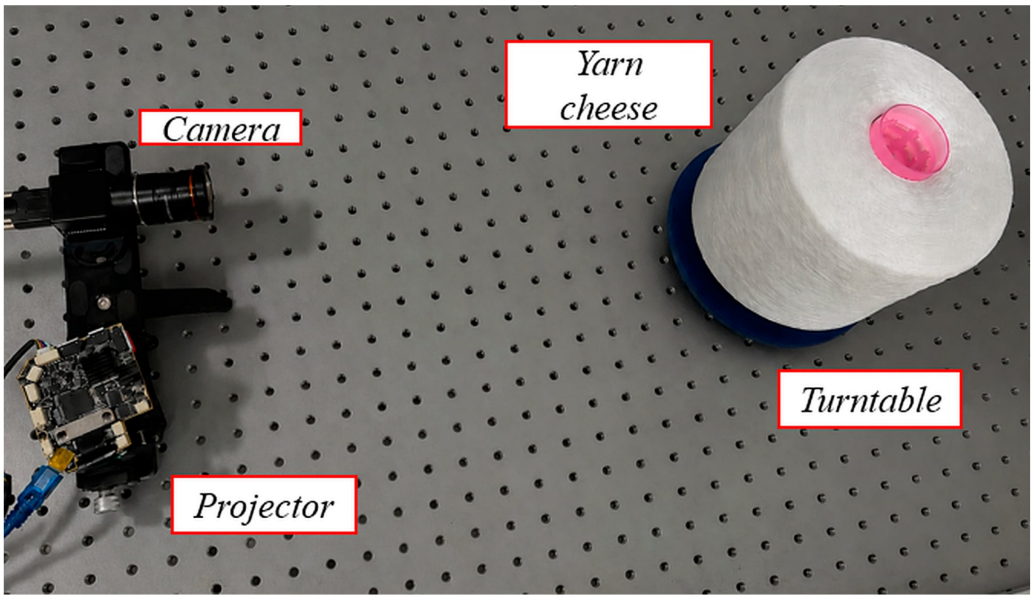


Figure 6. Experimental setup for yarn-cheese volume measurement based on monocular fringe projection structured light.

System calibration was performed using an 11 × 8 checkerboard calibration target with a square size of 15 mm. During calibration, the pose of the calibration target was adjusted within the common field of view of the camera–projector system, and multiple sets of calibration images were acquired. At each pose, the calibration target was kept stationary, while the projector sequentially projected black-and-white reference patterns and Gray-code patterns to obtain the data required for joint calibration. Meanwhile, to ensure stable decoding of the Gray-code patterns on the checkerboard surface, excessively large rotations of the calibration target were avoided to reduce the influence of projected-pattern distortion on the recovery of projector correspondences. Figure 7 shows the calibration result obtained by decoding the Gray-code patterns projected by the projector and captured by the camera.

As shown in Figure 7, the Gray-code encoded images are decoded along the horizontal and vertical directions to obtain the horizontal and vertical coordinate mappings of the projector, respectively. Although a limited number of discrete decoding points exist around the target region, the coordinate mappings were continuous within the calibration area, and the effective region was covered, satisfying the requirements for projector calibration and camera–projector joint optimization.

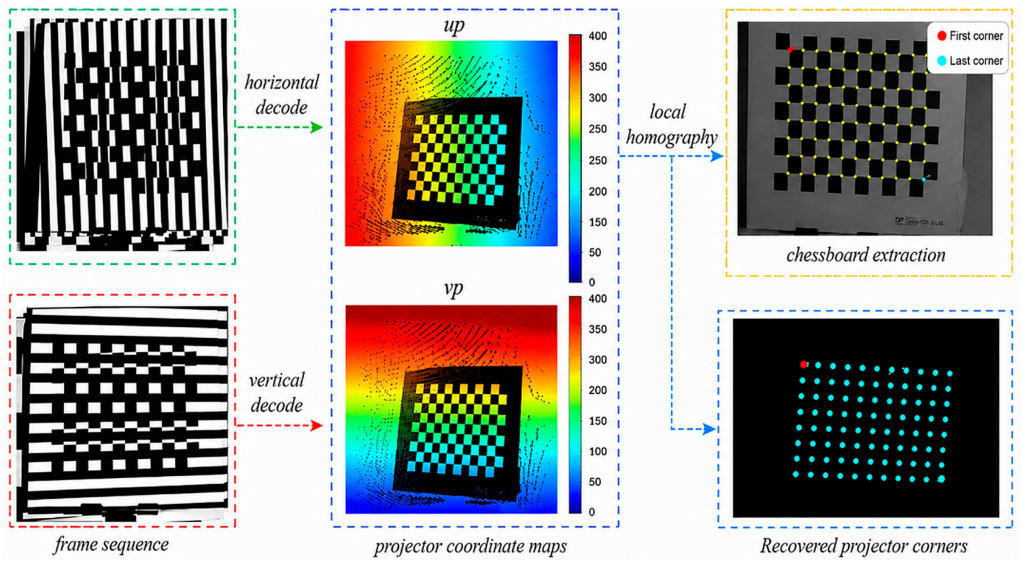


Figure 7. Projector point recovery from Gray-code decoding with dense correspondence mapping and local homography constraints.

Based on the recovered projector corners, the initial projector calibration was performed, achieving a reprojection error of 0.3090 pixels. After further camera–projector joint optimization, the system reprojection error was reduced to 0.1729 pixels. According to the spatial geometric relationship between the camera and projector after joint calibration, the optimal rotation matrix R and translation vector T between the camera and projector were calculated as follows:

$$R = \begin{bmatrix} 0.9909 & -0.0046 & 0.1346 \\ 0.0041 & 1.0000 & 0.0042 \\ -0.1346 & -0.0036 & 0.9909 \end{bmatrix}, \; T = \begin{bmatrix} -131.1323 \\ -0.4202 \\ 39.2553 \end{bmatrix}$$

Therefore, the baseline length between the camera and projector and the angle between their principal optical axes can be calculated as 136.8826 mm and 7.7428°, respectively.

3.2. Multi-View Structured-Light Point Cloud Registration

During the measurement process, the projector sequentially projected multi-frequency eight-step phase-shifting sinusoidal fringe patterns with spatial periods of 35, 36, and 37 onto the surface of the yarn cheese, and the industrial camera synchronously captured the corresponding structured-light images. The turntable was rotated with an angular interval of approximately 30°, and this acquisition process was repeated until a complete 360° scan was achieved. The single-view point cloud acquisition and registration results are shown in Figure 8.

Figure 8 shows that the side views capture the yarn-cheese surface. After registration, their fused contours are largely continuous.

Using Equations (1)–(7), the direction vector of the turntable rotation axis was calculated as $[-0.0172, -0.9955, 0.0931]$. The reference point on the rotation axis was determined as $[43.8929, 127.8647, 705.9056]$.

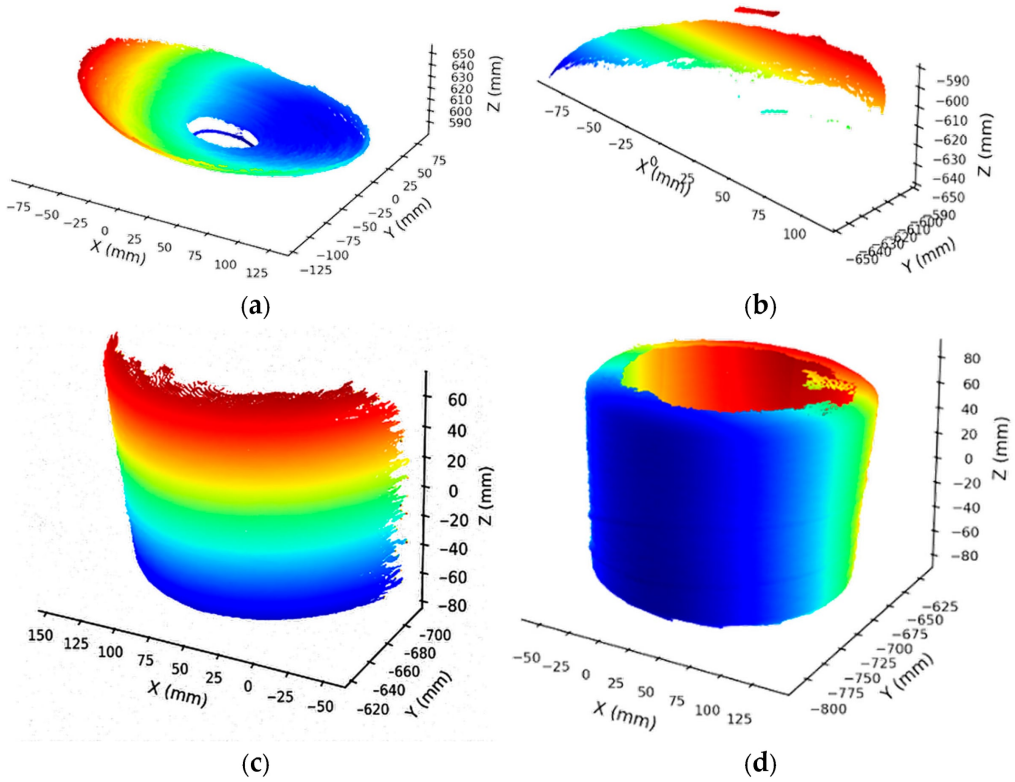


Figure 8. Multi-view structured-light point clouds: (**a**) bottom view; (**b**) top view; (**c**) registered side views; (**d**) complete fused point cloud.

After obtaining the above rotation-axis parameters, the side-view point clouds of the yarn cheese were transformed into the axis coordinate system, and the side-view registration result is shown in Figure 8c. To supplement the missing geometric information in the end regions, the top and bottom point clouds were separately acquired by adjusting the yarn-cheese orientation while maintaining the relative positions of the camera and projector unchanged, as shown in Figure 8a,b. Finally, the registered side point cloud was aligned with the top and bottom point clouds to obtain the complete yarn-cheese point cloud, as shown in Figure 8d.

Using the multi-view structured-light point clouds of the yarn-cheese side surface as the experimental data, the iterative closest point (ICP) method and its variants were compared with RA-SCR under the same initial poses obtained from coarse registration. The comparison results are shown in Figure 9.

Coarse alignment leaves local gaps and mismatches (Figure 9a). Conventional ICP variants can drift on similar yarn-cheese contours. RA-SCR restricts residual poses using the calibrated axis and shared cross-sectional geometry, producing a more continuous fused surface.

To evaluate the registration consistency of different methods, the side-view multi-view point cloud registration results obtained by ICP, point-to-point ICP (Pt-Pt), point-to-plane ICP (Pt-Pl), generalized iterative closest point (GICP), and RA-SCR were quantitatively evaluated under the same initial poses from coarse registration, point cloud preprocessing procedures, and downsampling scales [29]. The evaluation metrics included the mean fitness, residual registration error, and multi-view residual spatial deviation (MRSD). The results are summarized in Table 1. The method comparison in Table 1 and the ablation study in Table 2 used different yarn-cheese specimens. Their fitness values should therefore be interpreted within their respective experiments.

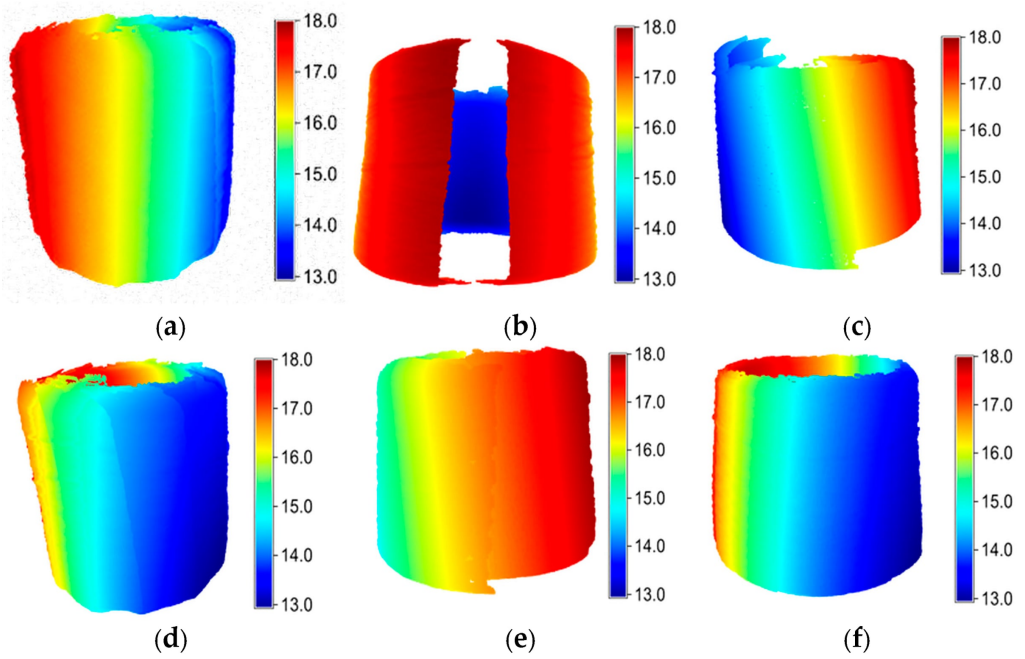


Figure 9. Multi-view registration results: (**a**) coarse alignment; (**b**) ICP; (**c**) point-to-point ICP; (**d**) point-to-plane ICP; (**e**) generalized iterative closest point (GICP); (**f**) RA-SCR.

Table 1. Comparison of multi-view reconstruction consistency.

MRSD (mm)	Correspondence RMSE (mm)	Mean Fitness	Method
4.5334	0.2425	0.3458	ICP
3.5342	0.1443	0.6422	Pt-Pt Registration
3.5148	0.1324	0.6831	Pt-Pl Registration
2.6124	0.0835	0.7582	GICP
1.3263	0.0452	0.8742	RA-SCR (Full Constraint Model)

Table 2. Ablation study of RA-SCR constraints. The specimen differs from that used in Table 1.

Radial STD (mm)	MRSD (mm)	Correspondence RMSE (mm)	Mean Fitness	Method
3.6214	4.5625	2.2388	0.3468	Initial Alignment
2.3359	2.5342	1.5124	0.4991	Axis-Prior Sequential ICP
1.8489	2.3223	1.0223	0.6117	Axis + 3-DoF Opt
1.5644	1.8875	0.2685	0.6863	Axis + 3-DoF + Shared Section (Global Radius)
1.0462	1.3256	0.0421	0.8775	RA-SCR (Full Constraint Model)

Different metrics were used to assess registration accuracy and geometric reconstruction. Registration performance was evaluated using fitness, correspondence RMSE, and multi-view residual spatial deviation (MRSD). For experiments with known reference poses, angular and translational errors were also calculated. The reconstructed cross-sectional geometry was assessed using radius-profile RMSE, model-radius RMSE, and the radial stan-

dard deviation within axial slices. Volume measurement errors were reported as absolute relative differences from the corresponding reference values.

Table 1 shows that the conventional iterative closest point (ICP) algorithm achieved a mean fitness of only 0.3458, with correspondence RMSE and MRSD values of 0.2425 mm and 4.5334 mm, respectively, indicating that it is difficult to establish stable multi-view correspondences for yarn cheeses with approximately axisymmetric structures. The evaluation metrics of other ICP variants were improved compared with the conventional ICP method; however, certain residual deviations remained. In contrast, RA-SCR increased the mean fitness to 0.8742 and reduced the correspondence RMSE and MRSD values to 0.0452 mm and 1.3263 mm, respectively, outperforming all other registration methods. The lower RMSE and MRSD indicate closer agreement among the registered views.

To verify the effectiveness of each key constraint module in RA-SCR, an ablation study was conducted by progressively introducing the rotation-axis constraint, three-degree-of-freedom (3-DoF) optimization, and shared-cross-sectional consistency constraint. In addition, radial standard deviation (Radial STD) was introduced to evaluate the mean radial spread of each axial slice after the fused point cloud was divided along the rotation-axis. The results are presented in Table 2.

In the initial coarse registration, the MRSD was 4.5625 mm, correspondence RMSE was 2.2388 mm, and Radial STD was 3.6214 mm. With the progressive introduction of the rotation-axis constraint, three-degree-of-freedom optimization, and shared-cross-sectional consistency constraint, the mean fitness continuously increased, whereas the correspondence RMSE and MRSD values continuously decreased. The final configuration had the highest mean fitness (0.8775) and the lowest correspondence RMSE (0.0421 mm), MRSD (1.3256 mm), and Radial STD (1.0462 mm).

In Table 2, axis-prior sequential ICP uses the calibrated axis for coarse initialization while retaining a conventional 6-DoF ICP refinement. It is distinct from axis + 3-DoF correspondence-only, which enforces the calibrated axis during optimization and serves as the equivalent-axis baseline in Tables 3–5. Axis + 6-DoF ICP is retained as the conventional baseline in the reduced-overlap test of Table 6.

Table 3. Controlled ablation of the shared-cross-section representation. N/A means not applicable.

Radius-Profile RMSE (mm)	Model-Radius RMSE (mm)	Translation RMSE (mm)	Angle RMSE (deg)	Method
0.1390	N/A	0.2220	0.8390	Axis + 3-DoF correspondence-only
0.1540	3.2260	0.2220	0.8380	Joint + global radius
0.0690	0.7430	0.2210	0.8380	Joint + layered radii

Table 4. Controlled comparisons With equivalent axis-prior and cross-section baselines.

Volume Error (%)	Radius-Profile RMSE (mm)	Translation RMSE (mm)	Angle RMSE (deg)	Method
A. Fine yarn cheese: held-out low-overlap benchmark				
0.3145	0.1121	0.1630	0.9274	Axis + 3-DoF correspondence-only
0.3870	0.0702	0.1385	0.9646	Fixed layered radii
0.2914	0.0623	0.1450	0.9135	Joint layered RA-SCR

Table 4. *Cont.*

Volume Error (%)	Radius-Profile RMSE (mm)	Translation RMSE (mm)	Angle RMSE (deg)	Method
B. Coarse yarn cheese: controlled volume benchmark				
0.2271	0.1773	0.2876	1.0210	Axis + 3-DoF correspondence-only
0.0641	0.3033	0.2875	1.0216	Joint + global radius
0.0289	0.1285	0.2891	1.0265	Joint layered RA-SCR

Note: Volume errors in Panel A were calculated using the internal controlled reference, whereas those in Panel B were calculated relative to FreeScan measurements.

Table 5. High-overlap, near-constant-radius results using original measured point clouds (20 controlled trials; mean values from five paired repeats per method).

Volume Error (%)	Radius-Profile RMSE (mm)	Translation RMSE (mm)	Method
0.1600	0.1661	0.3535	Axis-prior sequential ICP
0.0708	0.1563	0.2053	Axis + 3-DoF correspondence-only
0.0781	0.1575	0.1800	Fixed layered radii
0.0635	0.1480	0.2137	Joint layered RA-SCR

Table 6. Held-out low-overlap and initialization-perturbation results (39 conditions per method).

Volume Error (%)	Radius-Profile RMSE (mm)	Success Rate (%)	Successful Registrations	Method
0.3664	0.5575	87.1795	34/39	Joint layered RA-SCR
0.4284	0.5711	84.6154	33/39	Fixed layered radii
0.5951	0.6436	79.4872	31/39	Axis + 3-DoF correspondence-only
1.1801	1.3617	66.6667	26/39	Axis + 6-DoF ICP

3.2.1. Controlled Ablation and Comparison Under Equivalent Axis Constraints

To isolate the roles of the correspondence and layered radial terms, the controlled benchmark used twelve original side-view point clouds independently acquired from the same fine yarn cheese as the turntable was rotated through the recorded nominal angles. Each frame was captured separately. For reproducible comparisons, the same visibility masks, sampling-density settings, and Gaussian point perturbations with a standard deviation of 0.18 mm were applied to the corresponding acquired frames for all methods. The benchmark therefore preserves the real multi-view acquisition data while providing identical controlled overlap and perturbation conditions for mechanism isolation and error-propagation analysis.

A radial-only test was first performed in three angular-initialization trials (Trials 1–3). All trials converged to the same radial objective (29.6300) and radial standard deviation (1.0982 mm), while the angle-change RMSE remained between 6.6500 deg and 6.8210 deg and the final angle standard deviation ranged from 5.6700 deg to 6.3900 deg. This confirms that the radial term does not identify rotation about the axis and that spatial correspondences are required for angular estimation.

As shown in Table 3, replacing one global radius with layered radii reduced the model-radius RMSE from 3.2260 mm to 0.7430 mm (77.0%) and radius-profile RMSE from 0.1540 mm to 0.0690 mm (55.2%). The angular and translational errors changed only

slightly. The result therefore isolates the value of the axial shape representation rather than attributing the improvement to a different pose model.

For the held-out comparison, all methods shared the same calibrated axis, pose initialization, correspondence strategy, and optimization settings. The axis + 3-DoF correspondence-only baseline set the radial residual multiplier to zero. The fixed layered baseline estimated a shared center and 16 layer radii once from the coarsely aligned views and then held these cross-sectional parameters fixed while optimizing only the 3-DoF poses. Joint layered RA-SCR updated the poses, shared center, and layer radii together. The radial residual multiplier and number of axial layers were selected only on the standard-overlap validation split from multipliers {0.04, 0.08, 0.12, 0.16, 0.20} and layer counts {6, 8, 10, 12, 16}. Among settings causing no more than 0.5% degradation in angle, translation, inlier RMSE, or reference-nearest-neighbor RMSE relative to the 3-DoF correspondence-only baseline, the setting with the lowest validation radius-profile RMSE was selected. This yielded a radial residual multiplier of 0.20 and 16 layers, which were frozen before evaluation on the held-out low-overlap split with a 55 deg visible half-angle.

A second controlled benchmark used the original measured point-cloud data of a coarse yarn cheese to examine propagation from registration to volume. Twelve controlled view subsets were prepared with the same fixed trial configuration, the recorded nominal angles, fixed visibility and sampling-density conditions, and 0.18 mm Gaussian point perturbations. Axis + 3-DoF correspondence-only, joint global-radius optimization, and joint layered RA-SCR used the same calibrated axis, 3-DoF pose model, initialization, robust correspondence term, and fixed-cap volume calculation. A supplied FreeScan volume of 3462.3210 cm^3 for the same sample was used only as an external evaluation reference and was not used for pose estimation or parameter selection.

Panel A of Table 4 separates the contribution of jointly updating the cross-sectional parameters from merely supplying a layered shape prior. Relative to the fixed layered baseline, joint layered RA-SCR reduced the angular RMSE from 0.9646 deg to 0.9135 deg (5.3%), radius-profile RMSE from 0.0702 mm to 0.0623 mm (11.3%), and fixed-cap volume error from 0.3870% to 0.2914% (24.7%). The translation RMSE increased slightly from 0.1385 mm to 0.1450 mm, a difference of 0.0065 mm; thus, joint optimization did not improve every pose component. Relative to the axis + 3-DoF correspondence-only baseline, joint layered RA-SCR reduced the angular RMSE from 0.9274 deg to 0.9135 deg, translation RMSE from 0.1630 mm to 0.1450 mm, radius-profile RMSE from 0.1121 mm to 0.0623 mm, and volume error from 0.3145% to 0.2914%. The correspondence-based local-fit measures remained similar across the three methods. The principal additional value of joint updating is therefore more accurate axial-profile recovery and downstream volume estimation under reduced overlap, with a modest improvement in angular recovery, rather than uniform dominance in every local fit metric.

Panel B provides the corresponding registration-to-volume result for the coarse yarn cheese. With the 3462.3210 cm^3 FreeScan reference, the estimated volumes were 3454.4580 cm^3 for the axis + 3-DoF correspondence-only baseline, 3464.5390 cm^3 for the joint global-radius formulation, and 3463.3210 cm^3 for joint layered RA-SCR. The joint layered formulation produced the smallest absolute difference, 1.0000 cm^3, and the lowest relative error, 0.0289%, compared with 2.2180 cm^3 (0.0641%) and 7.8630 cm^3 (0.2271%), respectively. Its volume error was 54.9% lower than that of the global-radius formulation and 87.3% lower than that of the correspondence-only baseline. The pose metrics remained close across the three methods, indicating that the principal difference appears in propagation to the final integrated volume rather than in a uniformly large improvement of every local registration metric.

The results for the high-overlap, near-constant-radius condition are summarized in Table 5. The evaluation was performed over 20 controlled trials using the original measured point clouds.

3.2.2. Robustness Under Reduced Overlap and Initialization Perturbations

The mechanism study was complemented by a held-out low-overlap and initialization-error experiment using three original measured yarn-cheese point clouds that were not used for parameter selection. For each sample, controlled partial-view subsets were prepared from the measured points at view intervals of 30°, 45°, 60°, 75°, and 90°. Independent angular perturbations of ±1°, ±3°, and ±5° and transverse translation perturbations of 0.5, 1, and 2 mm were applied to the initial poses. Axis + 6-DoF ICP, axis-constrained 3-DoF correspondence-only optimization, fixed layered radii, and joint layered RA-SCR received the same point sets and perturbations. The 6-DoF ICP used its own staged ICP schedule; the three 3-DoF methods shared their correspondence settings and initial optimization stage.

The test conditions were divided into two groups for each of the three yarn-cheese samples. In the first group, five view intervals (30°, 45°, 60°, 75°, and 90°) were tested with angular and transverse translation perturbations fixed at 3° and 1 mm, respectively. In the second group, the view interval was fixed at 60°, and eight additional combinations were selected from angular perturbations (1°, 3°, and 5°) and translation perturbations (0.5, 1, and 2 mm), excluding the (3°, 1 mm) combination already included in the first group. This resulted in 13 distinct conditions per sample and 39 conditions per method. All methods were evaluated using the same test conditions, and registration success was determined by the criteria described below.

For this controlled benchmark, a trial was classified as successful only when the numerical procedure terminated normally with finite output, every adjacent view pair retained at least eight bidirectional nearest-neighbor inliers within 3.0 mm, the overlap-region RMSE did not exceed 1.2 mm, the radius-profile RMSE did not exceed 1.0 mm, and the relative volume error did not exceed 3.0%. The angular and translational perturbations defined the initialization difficulty and were not used as success thresholds. This definition was used only for the controlled benchmark with known references and is not an online acceptance criterion for practical measurements.

As shown in Table 6, RA-SCR successfully registered 34 of the 39 test cases (87.2%), compared with 33 for the fixed layered method (84.6%), 31 for the correspondence-only method (79.5%), and 26 for 6-DoF ICP (66.7%). RA-SCR also achieved the lowest mean radius-profile RMSE (0.5575 mm) and volume error (0.3664%). At the largest view interval of 90°, it succeeded in all three cases, whereas 6-DoF ICP failed in all three. These results show improved robustness over conventional ICP, although the success rate was only slightly higher than that of the fixed layered method.

3.3. Geometric Parameter and Volume Measurement Results of the Yarn Cheese

We measured five yarn cheeses to assess repeatability. Each sample was measured 20 times. Figure 10 summarizes the top and bottom radii, height, and total package volume.

The repeated measurements in Figure 10 show similar values for each sample's radii, height, and total volume. Table 7 compares these measurements and the wound-yarn volumes across the five samples.

Table 7 reports maximum relative errors of 1.5699% for the top radius, 1.8697% for the bottom radius, 2.3994% for the height, and 3.4625% for the total package volume. Subtracting bobbin volume gives a maximum wound-yarn-volume error of 2.8327%. All reported errors are below 4%.

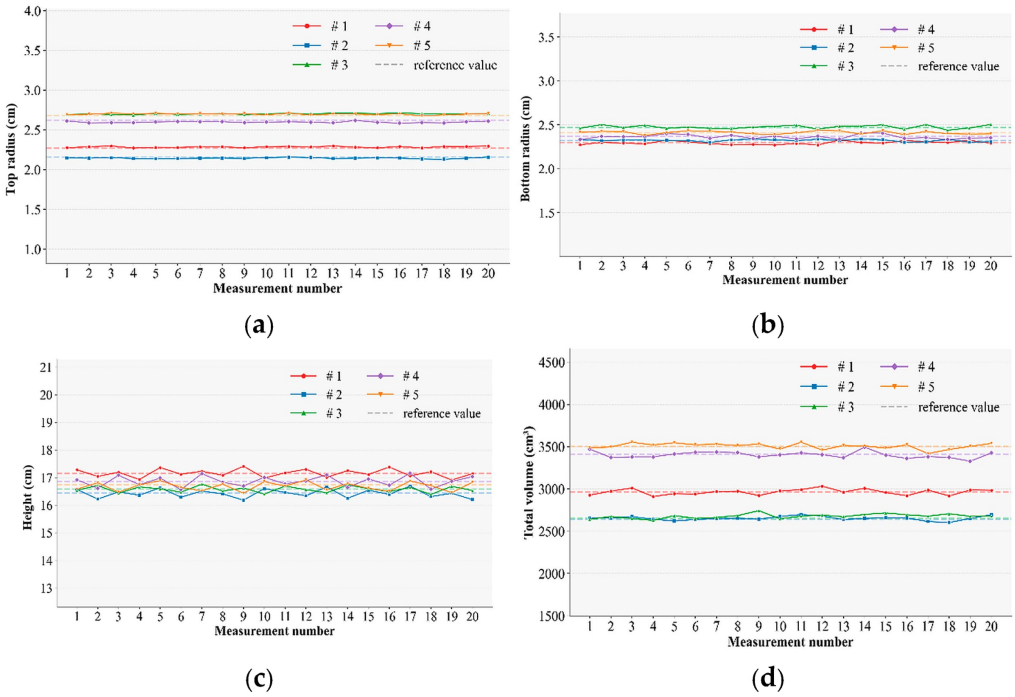


Figure 10. Repeated measurements of five yarn-cheese samples. Labels 1–5 denote samples 1–5, respectively; each sample was measured 20 times. (**a**) Top radius; (**b**) bottom radius; (**c**) height; (**d**) total yarn-cheese volume.

We also compared reconstructed surfaces from a separate set of yarn cheeses with FreeScan measurements (Figure 11).

FreeScan measurements were used as references in Table 8.

Across the yarn cheeses in Table 8, mean relative differences from FreeScan were 1.1884% for the top radius, 0.9924% for the bottom radius, 1.4391% for the height, and 3.1667% for the total volume. All were below 4%.

Several factors may contribute to the differences between the proposed method and the FreeScan measurements in Table 8. Errors in camera–projector calibration and phase recovery affect the reconstructed 3D coordinates, while inaccuracies in rotation-axis estimation and point cloud registration may introduce deviations in the recovered axial and radial profiles. In addition, surface fuzz and incomplete observations near the package ends can affect boundary detection and cross-sectional radius estimation.

Table 7. Measurement results and relative errors of yarn-cheese parameters.

5#	4#	3#	2#	1#	Measurement Category	Parameter
2.6854	2.6250	2.6856	2.1657	2.2752	Manual measurements (cm)	Top radius
2.7123	2.5912	2.7202	2.1317	2.2504	Measured results (cm)	
1.0017	1.2876	1.2884	1.5699	1.0900	Relative errors (%)	
2.4156	2.3748	2.4710	2.3218	2.3540	Manual measurements (cm)	Bottom radius
2.3830	2.4115	2.5172	2.3450	2.3305	Measured results (cm)	
1.3496	1.5454	1.8697	0.9992	0.9983	Relative errors (%)	
15.9210	16.1551	16.6372	15.7469	16.3250	Manual measurements (cm)	Height
16.2106	16.4774	17.0364	16.0883	16.5803	Measured results (cm)	
1.8190	1.9950	2.3994	2.1680	1.5639	Relative errors (%)	

Table 7. *Cont.*

5#	4#	3#	2#	1#	Measurement Category	Parameter
3501.3785	3412.3204	2656.2940	2644.7261	2963.5241	Manual measurements (cm^3)	Total volume of the yarn cheese
3584.4058	3315.7845	2741.3926	2553.1525	3043.7823	Measured results (cm^3)	
2.3713	2.8290	3.2037	3.4625	2.7082	Relative errors (%)	
3062.5428	2876.7408	2197.2802	2268.1028	2638.6672	Manual measurements (cm^3)	Wound-yarn volume
3149.2958	2798.0775	2252.4176	2213.4057	2708.9010	Measured results (cm^3)	
2.8327	2.7345	2.5093	2.4116	2.6617	Relative errors (%)	

Note: The yarn cheese was replaced between measurement sets; the empty-bobbin volume used for each wound-yarn volume calculation was obtained from the corresponding bobbin dimensions, rather than the yarn-cheese end radii listed in this table. Relative errors were calculated using the corresponding manual measurements as reference values.

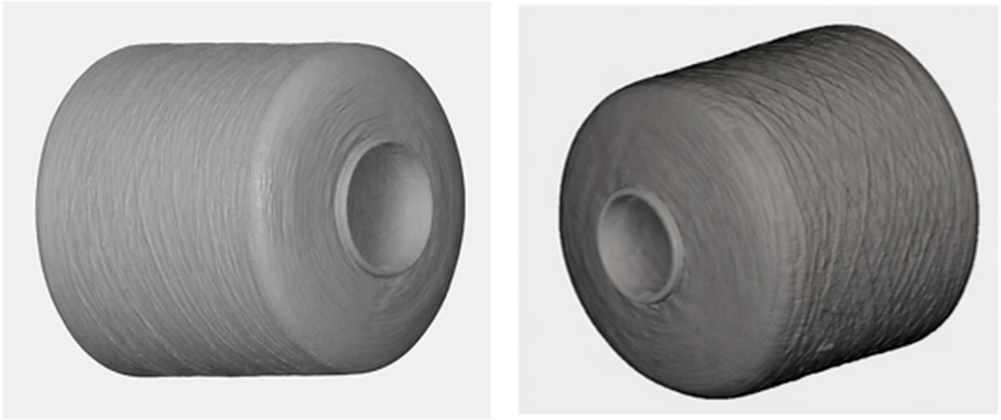


Figure 11. Comparison of reconstructed yarn-cheese surfaces: (**a**) FreeScan 3D scan; (**b**) proposed monocular structured-light reconstruction.

These errors can propagate to the final volume measurement. Since the total package volume is calculated by integrating the cross-sectional areas along the rotation axis, a small radius error δr produces an approximate volume error of $2\pi r \Delta z \delta r$ for a slice of thickness Δz and radius r. Errors in the estimated package height and bobbin dimensions also affect the calculated wound-yarn volume. Improving system calibration, maintaining stable turntable rotation, and obtaining more complete end-view point clouds may help reduce these errors. The comparison with FreeScan provides a reference for evaluating the measurement accuracy of the proposed method under the tested conditions.

Table 8. Comparison with FreeScan on geometric parameters and volume.

Mean	5#	4#	3#	2#	1#	Measurement Category	Parameter
2.3626	2.3158	2.3804	2.3793	2.2757	2.5852	FreeScan measurements (cm)	Top radius
2.3723	2.3506	2.4107	2.3504	2.2576	2.5553	Proposed method measurements (cm)	
1.1884	1.5027	1.2729	1.2146	0.7954	1.1566	Relative differences (%)	
3.4342	3.3760	3.4605	3.4365	3.3675	3.5421	FreeScan measurements (cm)	Bottom radius
3.4563	3.3985	3.5147	3.4610	3.3286	3.5726	Proposed method measurements (cm)	
0.9924	0.6665	1.5662	0.7129	1.1552	0.8611	Relative differences (%)	

Table 8. *Cont.*

Mean	5#	4#	3#	2#	1#	Measurement Category	Parameter
16.7435	16.6775	16.8534	16.5812	16.4353	17.1552	FreeScan measurements (cm)	Height
16.9835	16.8424	17.1708	16.7700	16.6921	17.4335	Proposed method measurements (cm)	
1.4391	0.9888	1.8833	1.1386	1.5625	1.6222	Relative differences (%)	
3237.4675	3037.0586	3337.5704	3262.5136	2983.5402	3566.3542	FreeScan measurements (cm^3)	Volume
3339.1763	3151.8575	3412.6542	3384.2245	3071.1407	3678.2435	Proposed method measurements (cm^3)	
3.1667	3.7799	2.2497	3.7306	2.9361	3.1373	Relative differences (%)	

4. Discussion

The controlled experiments separate two effects. Replacing a single global radius with an axially layered profile produced the larger reduction in profile error, whereas jointly updating the profile and residual poses provided a smaller additional benefit. The joint formulation is therefore not interpreted as uniformly improving pose accuracy.

The role of joint updating is more specific. Spatial correspondences retain the angular information needed to estimate rotation about the calibrated axis. The layered radial residual constrains transverse translations, the shared center, and the axial radii. Unlike a fixed-prior pipeline, the profile remains adjustable during registration: corrected poses update the profile, and the current shared profile regularizes subsequent pose updates. This coupling can improve profile recovery even when individual pose metrics change only modestly.

RA-SCR is positioned within the broader family of joint pose-shape estimation methods rather than as a general replacement for them. Its task-specific distinction is the combination of calibrated-axis three-degree-of-freedom residual poses with a shared layered cross-sectional profile for approximately axisymmetric yarn packages. Lv et al. [21] used local circular cross-sections for coarse registration of tubular structures and then applied coherent point drift for refinement. RA-SCR instead keeps the layered profile inside the multi-view objective throughout refinement. Lai et al. [24] used graph optimization to improve global consistency in multi-view structured-light reconstruction, whereas RA-SCR uses the calibrated turntable axis and shared radial geometry to constrain the residual registration.

The reduced-overlap experiment indicates that the proposed coupling can be beneficial when correspondence information becomes incomplete. The methods produced similar errors at easy and moderate view intervals, but RA-SCR achieved the highest overall success rate (87.1795%) and satisfied the predefined success criteria in all three cases at the 90° view interval, whereas 6-DoF ICP did not meet these criteria in any of the three cases. Under reduced overlap, the radial constraint helps stabilize transverse alignment and the recovered cross-sectional profile, while the correspondence term remains responsible for angular estimation. This property is useful when adjacent views contain repeated yarn texture, missing regions near the package ends, or an imperfect initial pose.

The volume comparisons should be interpreted separately from pose accuracy. All methods used the same downstream volume calculation, so the reported differences reflect the combined result of registration, recovered axial profile, boundary extraction, and integration. However, these comparisons do not isolate the contribution of pose-estimation accuracy to the observed reduction in volume error. Rather, under the controlled processing used here, the coupled formulation was associated with a more consistent layered profile and a lower final volume error.

The current implementation assumes an approximately axisymmetric package, a stable calibrated turntable axis, and sufficient side-view overlap to establish spatial correspondences. Strong ellipticity, local collapse, highly asymmetric winding, or axis drift can violate

these assumptions. Surface fuzz and incomplete top or bottom coverage also affect the representative slice radius, particularly near the package ends. The validation set remains limited to the yarn cheeses and perturbation ranges reported here, and FreeScan was used as an external reference rather than an independent traceable standard. These limitations define the scope of the present conclusions.

The robustness of geometric fitting also depends on the quality of the acquired point clouds. Bao et al. [25] investigated Huber-loss-based fitting and denoising for cross-sectional point-cloud data, highlighting the relevance of robust estimation in geometric modeling. In RA-SCR, the Huber loss is applied to correspondence and radial residuals to reduce the influence of outliers. However, robust loss functions cannot fully compensate for systematic errors caused by an inaccurate rotation axis or strongly noncircular cross-sections.

Further work should examine more yarn counts, package densities, taper angles, and deliberately non-axisymmetric defects, with independently repeated axis calibration and reference measurements. Modeling axis uncertainty within the optimization would help determine when recalibration is necessary. More complete end-view acquisition or an explicit end-surface model could reduce sensitivity to missing boundary data. The same framework may also be applicable to other wound or rolled products, but that extension should be tested rather than assumed. For production use, computation time and automatic checks for registration failure will also need to be evaluated.

5. Conclusions

RA-SCR was developed for multi-view structured-light measurement of yarn-cheese volume. The calibrated turntable axis restricts each view to a three-degree-of-freedom residual pose, and these poses are updated together with a shared layered cross-sectional profile. Spatial correspondences supply the angular information, while the layered radial term regularizes the cross-view profile. Axial–radial integration yields the total package volume, and bobbin subtraction yields the wound-yarn volume.

In the controlled fine-yarn experiment, RA-SCR achieved a radius-profile RMSE of 0.0623 mm and a fixed-cap volume error of 0.2914%. In the reduced-overlap tests, RA-SCR achieved an overall registration success rate of 87.1795%. Across five yarn cheeses, the maximum relative errors were 3.4625% for total package volume and 2.8327% for wound-yarn volume, while the mean total-volume difference from FreeScan was 3.1667%. These results support the use of RA-SCR for the approximately axisymmetric packages and acquisition conditions tested here; broader validation is still required for other package shapes and operating conditions.

Author Contributions: Conceptualization, C.L. and Y.X.; methodology, C.L.; software, C.L.; validation, C.L.; formal analysis, C.L.; investigation, C.L.; resources, Y.X.; data curation, C.L.; writing—original draft preparation, C.L.; writing—review and editing, C.L. and Y.X.; visualization, J.L.; supervision, Y.X.; project administration, Y.X.; funding acquisition, Y.X. All authors have read and agreed to the published version of the manuscript.

Funding: This study was supported by the Zhejiang Province Natural Science Foundation of China (LQ20F030019) and Zhejiang Province Public Welfare Technology Application Research Project (LGG22E050051).

Data Availability Statement: Data underlying the results presented in this paper are not publicly available at this time but may be obtained from the authors upon reasonable request. The source code for this study is publicly available at https://github.com/weiyang2333/RA-SCR-yarn-cheese-volume-measurement-structured-light, acccessed on 16 November 2026.

Conflicts of Interest: The authors declare no conflicts of interest.

References

1. Zhang, H.; Lin, X.; Zhai, Z.; Wu, J.; Zhang, C. A constant residual tension control method for the precision winding of yarns. *Text. Res. J.* **2025**, *95*, 2420–2436. [CrossRef]
2. Gramsch, S.; Bell, E.G.; Moghiseh, A.; Schmeißer, A. Analysis of the package diameter in winding processes by image analysis and a linear regression model. *J. Eng. Fibers Fabr.* **2022**, *17*, 1–10. [CrossRef]
3. Schmeißer, A.; Bell, E.G.; Gramsch, S.; Heidenreich, R. Simulation-based setting suggestions for yarn winding units to reduce color variation in knitted fabric. *Text. Res. J.* **2023**, *93*, 2604–2619. [CrossRef]
4. Haleem, N.; Bustreo, M.; Del Bue, A. A computer vision based online quality control system for textile yarns. *Comput. Ind.* **2021**, *133*, 103550. [CrossRef]
5. Tran, D.T.; Dao, A.T.; Chu, D.H. Effect of technological winding parameters on yarn package density. *HaUI J. Sci. Technol.* **2024**, *60*, 135–142. [CrossRef]
6. Zhang, H.; Wang, J.; Wu, J.; Bian, H.; Wei, Y. Active tension control of the conical winding system based on the neural network control algorithm of radial-basis functions. *Text. Res. J.* **2023**, *93*, 3443–3458. [CrossRef]
7. Haleem, N.; Wang, X. Recent research and developments on yarn hairiness. *Text. Res. J.* **2015**, *85*, 211–224. [CrossRef]
8. Guo, M.; Gao, W.; Wang, J. Online measurement of sizing yarn hairiness based on computer vision. *Fibers Polym.* **2023**, *24*, 1539–1552. [CrossRef]
9. Matusiak, M.; Frącczak, Ł. Investigation of 3D woven fabric topography using laser-scanning. *Fibres Text. East. Eur.* **2018**, *26*, 81–88. [CrossRef]
10. Liang, D.; Li, D.; Yang, K.; Hu, W.; Chen, X.; Chen, Z. Scene measurement method based on fusion of image sequence and improved LiDAR SLAM. *Electronics* **2024**, *13*, 4250. [CrossRef]
11. Pasinetti, S.; Nuzzi, C.; Luchetti, A.; Zanetti, M.; Lancini, M.; De Cecco, M. Experimental procedure for the metrological characterization of time-of-flight cameras for human body 3D measurements. *Sensors* **2023**, *23*, 538. [CrossRef] [PubMed]
12. Siswantoro, J.; Asmawati, E.; Siswantoro, M.Z.F.N. A rapid and accurate computer vision system for measuring the volume of axi-symmetric natural products based on cubic spline interpolation. *J. Food Eng.* **2022**, *333*, 111139. [CrossRef]
13. Huynh, T.T.M.; TonThat, L.; Dao, S.V.T. A vision-based method to estimate volume and mass of fruit/vegetable: Case study of sweet potato. *Int. J. Food Prop.* **2022**, *25*, 717–732. [CrossRef]
14. Tan, J.; He, Z.; Su, W.; Dong, B.; Bai, Y.; Lei, L. Robust fringe projection measurement based on reference phase reconstruction. *Opt. Lasers Eng.* **2021**, *147*, 106746. [CrossRef]
15. Xu, P.; Zhang, L.; Shan, S.; Wang, J. Efficient and robust 3D reconstruction: Absolute phase extraction algorithm based on three gray images. *Opt. Lasers Eng.* **2024**, *180*, 108334. [CrossRef]
16. Zhu, Z.; Zhou, Y.; Lu, W.; Zhang, J.; Zhou, L.; Liu, H. Robust structured light 3D measurement method based on polarization-encoded projection patterns. *Appl. Opt.* **2024**, *63*, 210–220. [CrossRef] [PubMed]
17. Wang, B.; Chen, W.; Qian, J.; Feng, S.; Chen, Q.; Zuo, C. Single-shot super-resolved fringe projection profilometry (SSSR-FPP): 100,000 frames-per-second 3D imaging with deep learning. *Light Sci. Appl.* **2025**, *14*, 70. [CrossRef] [PubMed]
18. Zhao, Y.; Yu, H.; Zheng, Y.; Zhang, Y.; Zheng, D.; Han, J. Scene-adaptive pattern coding-based fringe projection profilometry: Diffuse surfaces identification and 3-D reconstruction in cluttered scenes. *Opt. Express* **2023**, *31*, 32565–32581. [CrossRef] [PubMed]
19. Qin, Z.; Yu, H.; Wang, C.; Guo, Y.; Peng, Y.; Ilic, S.; Hu, D.; Xu, K. GeoTransformer: Fast and robust point cloud registration with geometric transformer. *IEEE Trans. Pattern Anal. Mach. Intell.* **2023**, *45*, 9806–9821. [CrossRef] [PubMed]
20. Yang, J.; Zhang, X.; Wang, P.; Guo, Y.; Sun, K.; Wu, Q.; Zhang, S.; Zhang, Y. MAC: Maximal cliques for 3D registration. *IEEE Trans. Pattern Anal. Mach. Intell.* **2024**, *46*, 10645–10662. [CrossRef] [PubMed]
21. Lv, Y.; Kang, C.; Liu, J.; Zhou, H. A point cloud registration method for steel tubular arch rib segments of CFST arch bridges based on local geometric constraints. *Buildings* **2025**, *15*, 2130. [CrossRef]
22. Feng, W.; Qu, T.; Gao, J.; Wang, H.; Li, X.; Zhai, Z.; Zhao, D. 3D reconstruction of structured light fields based on point cloud adaptive repair for highly reflective surfaces. *Appl. Opt.* **2021**, *60*, 7086–7093. [CrossRef] [PubMed]
23. Feng, Y.; Wu, R.; Li, P.; Wu, W.; Lin, J.; Liu, X.; Chen, L. Multi-view high-dynamic-range 3D reconstruction and point cloud quality evaluation based on dual-frame difference images. *Appl. Opt.* **2024**, *63*, 7865–7874. [CrossRef]
24. Lai, Z.; Zhang, R.; Wang, X.; Zhang, Y.; Jia, Z.; Han, S. Fully automated structured light scanning for high-fidelity 3D reconstruction via graph optimization. *Opt. Express* **2024**, *32*, 9139–9160. [CrossRef] [PubMed]
25. Bao, Y.; Li, S.; Tang, C.; Sun, Z.; Yang, K.; Wang, Y. Research on fitting and denoising subway shield-tunnel cross-section point-cloud data based on the Huber loss function. *Appl. Sci.* **2025**, *15*, 2249. [CrossRef]
26. Ye, J.; Xia, G.; Liu, F.; Cheng, Q. 3D reconstruction of line-structured light based on binocular vision calibration rotary axis. *Appl. Opt.* **2020**, *59*, 8272–8278. [CrossRef] [PubMed]
27. Li, Z.; Wang, Z.; Huang, J.; Duan, Q.; Qi, M.; Gao, J.; Wang, W.; Dong, Q.; Li, Q.; Ai, S. Blade profile extraction and edge completion method based on structured light measurement point cloud. *Precis. Eng.* **2024**, *86*, 225–238. [CrossRef]

28. Huang, J.; Lian, D.; Lin, T.; Yang, R.; Liu, J.; Liu, Y.; Tan, J. Bidirectional line-structured light scanning measurement method for maximum thickness of aero-engine blade cross sections based on profile features. *IEEE Trans. Instrum. Meas.* **2024**, *73*, 5034710. [CrossRef]
29. Pomerleau, F.; Colas, F.; Siegwart, R.; Magnenat, S. Comparing ICP variants on real-world data sets: Open-source library and experimental protocol. *Auton. Robots* **2013**, *34*, 133–148.

Disclaimer/Publisher's Note: The statements, opinions and data contained in all publications are solely those of the individual author(s) and contributor(s) and not of MDPI and/or the editor(s). MDPI and/or the editor(s) disclaim responsibility for any injury to people or property resulting from any ideas, methods, instructions or products referred to in the content.